Journal of
Materials Chemistry A

PAPER

View Article Online
View Journal | View Issue

Cite this: *J. Mater. Chem. A*, 2026, **14**, 11540

Rational design of organic layer/3D silver foam electrodes for electrochemical CO_2 reduction reaction at diluted concentration

Kyeong-Nam Kang,†[ab] Dongyoon Shin,†[a] Jihoon Kim, †[a] Sang Heon Han,[a] Jiseon Kim,[a] Kyung Taek Woo,[c] Seoungsoo Park[c] and Yun Jeong Hwang *[ab]

Electrocatalysts for the electrochemical CO_2 reduction reaction (CO_2RR) have been developed for carbon neutrality by enabling the direct conversion of renewable resources into valuable carbon-based fuels and chemicals. Even electrocatalysts that exhibit high selectivity for CO_2RR at high CO_2 concentrations often suffer from increased competitive hydrogen production at lower CO_2 concentrations, requiring the investigation of catalysts that maintain stable selectivity across a wide concentration range. In this work, we fabricated a highly porous three-dimensional (3D) silver foam on an organic layer-added gas diffusion electrode. The porous 3D Ag foam exhibited the greatest improvement when combined with a benzimidazole organic layer (BI-*sf*), whose suitable CO_2-affinitive interfacial modifier and release facilitated CO_2 reduction pathways toward CO production on the Ag surface. These phenomena helped to enhance the partial current density (j_{CO}) and faradaic efficiency (FE) for CO production under diffusion-controlled regions. Compared with Ag nanoparticles (AgNP), the BI-*sf* electrocatalyst achieved a 4-fold and 2.5-fold increase in maximum j_{CO} with membrane-electrode-assembly (MEA) under 10% and 100% CO_2 concentration conditions, respectively. Additionally, when the CO_2 concentration decreased within 50–10%, BI-*sf* maintained relatively higher FE (CO) values compared to when BI was absent, demonstrating the promoting effect of BI under low concentrations of CO_2. These findings suggest that adjusting molecular interactions with CO_2 is particularly important to achieve high product selectivity in CO_2RR under low CO_2 concentrations for practical CO_2 utilization applications.

Received 23rd October 2025
Accepted 28th January 2026

DOI: 10.1039/d5ta08633g

rsc.li/materials-a

Introduction

The electrochemical carbon dioxide reduction reaction (CO_2RR) is promising for closing the anthropogenic carbon cycle because it converts CO_2 into value-added fuels or chemical feedstocks using renewable electricity.[1–3] Most of the CO_2RR performances have been investigated at highly purified CO_2 gas streams (>99% concentration) to increase reaction rates and suppress competitive side reactions, including the hydrogen evolution reaction (HER).[4–6] The concentrated CO_2 feed conditions can be utilized to understand the reaction activity and fundamental phenomena of CO_2RR, but their practical application may be limited because the costly CO_2 capture-and-regeneration process must be integrated upstream.[7,8] In flue gas or direct air CO_2 streams, the concentrations of CO_2 are 15–20%, and even lower in direct air scenarios (∼0.04%) where limited mass transfer may become the primary bottleneck due to low partial pressure of CO_2.[9,10] Developing an efficient electrocatalyst that can operate effectively at low CO_2 concentrations remains a challenge for scalable carbon utilization methods.

Recent efforts have concentrated on tuning catalyst surfaces, electrode architectures, and local microenvironments to address CO_2 mass-transfer limitations. Metal-based catalysts such as silver (Ag) and gold (Au) have excellent selectivity towards CO formation.[11–14] However, their performance declines significantly in a diluted CO_2 atmosphere due to limited CO_2 availability near active sites, while the competitive HER from water increases. In aqueous CO_2RR environments, suppressing HER is inherently crucial for achieving selective CO_2 conversion.[5,15–19] To this end, even in conditions of high concentrations of CO_2, various strategies have been demonstrated, including introducing porous gas diffusion electrodes (GDEs), controlling the hydrophilicity/hydrophobicity of the surface, designing defective nanostructures with high CO_2RR activity, or regulating microenvironments through ion accumulation or transport.[20–22] Nonetheless, these approaches often face issues related to limited durability, complex fabrication

---

[a] *Department of Chemistry, College of Natural Science, Seoul National University (SNU), Seoul 08826, Republic of Korea. E-mail: yjhwang1@snu.ac.kr*

[b] *Center for Nanoparticle Research Institute for Basic Science (IBS), Seoul 08826, Republic of Korea*

[c] *KOGAS R&D Institute, Korea Gas Corporation, Ansan-si, Gyeonggi-do, 15328, Republic of Korea*

† These authors contributed equally.

processes, or instability under high current densities, which require more refined strategies specialized at low-concentration conditions.[23,24]

Meanwhile, organic molecule-assisted interface engineering has emerged as a powerful method for controlling the local chemical environment and enhancing CO_2 adsorption on catalytic surfaces. Tailored organic modifiers can increase CO_2 affinity through dipole–quadrupole interactions or Lewis acid–base interactions, decrease the local proton concentration, and inhibit competitive HER processes.[25–28] Protonated organic cations have also garnered attention. They act as co-catalysts if introduced onto the surface of the cathode electrocatalyst under pure water electrolyte conditions due to their ability to activate CO_2 molecules instead of alkali cations.[29,30] In addition, amines or their derivatives have been widely investigated as CO_2 absorbents due to their rapid reaction rates, highly selective interaction with CO_2, and ability to be regenerated for repeated use.[31] Therefore, we propose that organic molecule layers can be effective components that increase interaction with CO_2, allowing efficient CO_2 utilization even under diluted conditions.

In this study, we report a facile fabrication of an organic molecule-modified 3D-Ag foam electrode that enables efficient electrochemical reduction of low-concentration CO_2 gas in a membrane electrode assembly (MEA) electrolyzer. The introduction of a CO_2-philic organic interlayer between the Ag catalyst and the GDE enhanced CO_2 adsorption and local concentration near active sites while effectively suppressing hydrogen evolution. The 3D porous structure of Ag foam further enhanced gas–liquid interface stability and electron transport, maintaining superior activity at high current densities (>200 mA cm^{-2}) even under 10% CO_2 conditions. Density functional theory (DFT) calculations combined with electrochemical performance confirmed that the molecular interlayer lowered the activation energy barrier for *COOH formation and promoted charge delocalization across the catalyst–electrolyte interface. The proposed electrode design offers several key advantages for industrial deployment. First, it is simple, solution-based, and compatible with large-area MEA configurations, making it highly scalable and cost-effective. Second, by enabling direct CO production from low-concentration CO_2, this technology can be integrated directly into existing carbon capture and utilization (CCU) infrastructure, particularly in sectors such as natural gas processing, biogas upgrading, and flue gas treatment at power or cement plants. Finally, the produced CO can be readily utilized as a component of syngas for downstream synthesis of fuels (methanol, Fischer–Tropsch hydrocarbons) and commodity chemicals, providing a sustainable pathway toward carbon neutrality.[32,33]

Experimental section

Chemicals/materials

All chemicals were used as received without further purification. Iridium(IV) oxide (Premion™, 99.99% (metals basis), Ir 84.5% min), silver nanopowder (APS 20–40 nm, 99.9% (metals basis)), silver sulfate (ACS, 98% min), L-histidine (98%+), benzimidazole (99%), 1H-benzotriazole (99%) were bought from Thermo Fisher Scientific. Sulfuric acid (99.999%), octylamine (99%), and sodium citrate tribasic dihydrate (puriss, p.a., ACS reagent, ≥99.0%) were purchased from Sigma-Aldrich. Common solvents and electrolytes, such as isopropyl alcohol, ethyl alcohol, potassium bicarbonate, and potassium hydroxide, were purchased from Samchun Chemicals or Daejung Chemicals & Metals. Deionized water (DW, Direct-Q, 18.2 MΩ cm) was used routinely.

Preparation of a three-dimensional silver foam on an organic layer-added gas diffusion electrode

Carbon paper and GDE electrodes (39BB, Sigracet) were cut into 36 mm × 25 mm and dried in an oven at 110 °C overnight before use. To investigate the effect of the organic-molecule layer beneath the Ag electrocatalyst on CO_2RR, organic molecules were first coated onto the GDE electrode. Various organic molecules, including benzimidazole (BI), L-histidine (HIS), benzotriazole (BTr), and octylamine (OA), were screened to determine the effect of the organic layer on CO_2RR performances. Each organic molecule, Nafion solution (D521, 5 wt% in ethanol), and isopropyl alcohol (IPA), were mixed in a 6 mg : 24 mg : 1 mL ratio, and were sonicated for ≥30 min to prepare the ink. Then, the ink was spray-coated onto a 25 mm × 25 mm portion of the GDE until a total loading amount of 0.32 mg cm^{-2}, unless stated otherwise. The spray-coated GDEs were subjected to Ag sputtering (15 W) for 210 s, resulting in a thin film (∼7 nm) covering the surface of the organic molecule-coated GDE and facilitating the electrodeposition of Ag foam. The back side of the GDE was sealed with tape, and the GDE was used as the working electrode during electrodeposition. For the electrodeposition, a 15 mm × 15 mm Pt mesh and a leakless Ag/AgCl electrode were used as the counter electrode and reference electrode, respectively. An aqueous bath of 20 mM silver sulfate with L-histidine (20 mM), sodium citrate tribasic dihydrate (0.1 M), and sulfuric acid (1.5 M) was used for the electrodeposition. A voltage of −4 V was applied for 30 s to enable porous Ag foam deposition *via* the dynamic hydrogen-bubble template (DHBT) method. The fabricated electrode was carefully washed in excess deionized water and dried thoroughly at 60 °C.

Material characterization

To analyze the surface morphology and elemental composition, scanning electron microscopy (SEM) and energy-dispersive X-ray spectroscopy (SEM-EDX) were undertaken using an Apreso 2 S Hivac SEM at an accelerating voltage of 10.0 kV. The crystalline nature of the silver foam was determined by X-ray diffraction (XRD; Bruker D2 Phaser diffractometer) using Cu Kα radiation ($\lambda = 1.5406$ Å). Diffraction patterns were collected in continuous mode over 20–80°. XPS analysis was performed using an Axis Supra+ (Kratos) system with Al Kα radiation. Infrared (IR) and Raman spectroscopy were applied to confirm the existence of benzimidazole after Ag sputtering. FT-IR spectra were collected on a PerkinElmer (Spectrum Two) spectrometer using a sample prepared by coating BI onto Ni foil and then Ag-sputtering to avoid spectral interference from carbon paper. Raman spectra were collected on a Renishaw (InVia Qontor) spectrometer.

Electrochemical CO_2RR measurements

CO_2RR experiments were conducted in a gas-fed membrane electrode assembly (MEA) electrolyzer (Dioxide Materials). The fabricated GDEs and platinized Ti meshes sprayed with IrO_2 ink were used as the cathode and anode, respectively. The two electrodes were separated by a pre-activated anion exchange membrane (AEM, Sustainion, Dioxide Materials) to construct a zero-gap MEA. The membrane was activated as instructed by Dioxide Materials before use. The anolyte (0.1 M $KHCO_3$) was pumped through the cell at a flow rate of 100 sccm using a peristaltic pump. Mass flow controllers (MFCs) of N_2 and CO_2 were adjusted to afford a total flow of 200 sccm, depending on the desired CO_2 conditions. The flow rates of high-purity CO_2 (99.999%) and N_2 (99.999%) gases were controlled by MFCs, which passed through a mixing chamber before being supplied to the MEA electrolyzer. The CO_2 concentration in the CO_2/N_2 gas mixture was confirmed by gas chromatography (GC, Agilent 8890). The gaseous products of CO_2RR were quantified using an online-connected GC equipped with a ShinCarbonST column (Restek), a thermal conductivity detector (TCD) and a flame ionization detector (FID). Liquid products were not detected by ^{1}H NMR spectroscopy (Varian 500 MHz spectrometer). Chronoamperometry (CA) and chrono-potentiometry (CP) measurements were carried out on an Ivium potentiostat (Ivium-n-Stat) or Biologic potentiostat (VMP-3e).

Calculation of partial charge

To determine the partial charge of different molecules, an iterative calculation procedure proposed by Gasteiger *et al.* was used.[34] Codes for calculation are available at: https://github.com/jihoonkim2000/Molecules_partialcharge.

DFT calculation

To calculate the CO_2 reduction ability of different molecules adsorbed on silver, a series of DFT calculations was conducted. DFT calculations were performed using Quantum Espresso software[35] following the generalized gradient approximation (GGA) scheme with the Perdew–Burke–Ernzerhof (PBE) functional.[36] A Grimme-D3 correction was introduced to describe the van der Waals interaction between atoms, and the projector-augmented wave (PAW) method was used to describe the behavior of core atoms with a cutoff energy of 450 eV.[37,38] For the screening of molecules *via* the *COOH adsorption energy descriptor, molecules and the *COOH adsorbate were placed on top of a 5 × 5 Ag monolayer with Γ-point Brillouin zone sampling. The organic molecule candidates varied: benzoxazole (BO), benzothiazole (BT), L-histidine (HIS), benzimidazole (BI), indole (In), benzopyrazole (BP), benzotriazole (BTr), imidazole (Im), pyridine (Py), and octylamine (OA). Meanwhile, for the simulation of the CO_2 reduction pathway on secondary amines, molecules were placed on top of a 4 × 4 × 2 silver slab with a frozen bottom layer, and the *c*-axis was set to 22 Å to prevent unwanted interactions along the axis. Brillouin zone sampling was done with Γ-centered 2 × 2 × 1 sampling. A Gaussian smearing of 0.2 eV was introduced to account for silver. For both simulations, the electronic convergence criteria and force convergence criteria were set to 10^{-6} eV and 0.05 eV Å^{-1}, respectively. The adsorption free energy was calculated using the following equation:

$$nG_{*\text{ads}} = G_{\text{system}} - G_{\text{adsorbate}} - G_{\text{slab}}$$

In which the following equation represents Gibbs free energy:

$$= E + \text{ZPE} - \text{TS} + \int C_{\text{p}}\text{d}T.$$

where G is the Gibbs free energy, E is the energy given by the density functional theory calculation, ZPE is the zero-point energy, T is the temperature, S is the entropy, and C_p is the heat capacity. The energy of molecules was calculated with a unit cell size of 20 × 20.5 × 21 Å^3 with single Γ-point Brillouin zone sampling.

Bond strength analysis with crystal orbital Hamilton population (COHP)

From the PAW-based DFT calculation results, COHP analysis was conducted to investigate the hydrogen bond strength between N–H⋯O. Calculations were done with the LOBSTER package.[39]

Results and discussion

Structural and interfacial characterization of the organic layer-assisted 3D-Ag foam

Fig. 1a shows the screening procedure for this work. For the initial screening of a vast chemical search space, molecules containing at least one of the 20 functional groups of interest were selected and analyzed using keyword queries in the Scopus database.[40] As a result, the amine group was selected based on the number of publications (keyword search results are summarized in Fig. S1). Afterward, based on the fact that aromatic molecules attach well to metallic surfaces *via* van der Waals interaction, most of the amines that we selected were molecules with aromaticity, except for octylamine as a molecule for comparison.[41] A list of 10 manually selected amines with their abbreviations is presented in Table S1. A candidate list of molecules contains aromatic, secondary amines to fully saturated, aliphatic amines, and from small (*e.g.*, pyridine) to bulky (*e.g.*, octylamine) molecules.

Enhancing local CO_2 availability at the electrode interface is a key factor in CO_2 electroreduction. Hence, we investigated the CO_2 affinity of candidate molecules using $\Delta G(*CO_2)$ as a descriptor for their potential role as CO_2-affinitive interfacial modifiers. Based on this criterion, 10 representative molecules were systematically compared. Fig. S2 shows the adsorption free energy of the molecular CO_2 physisorbed on a molecule adsorbed on the Ag surface. As expected, all the molecules except for OA (octylamine) exhibited similar CO_2 adsorption capability, while OA exhibited significantly lower CO_2 adsorption capability due to the lack of van der Waals interaction with

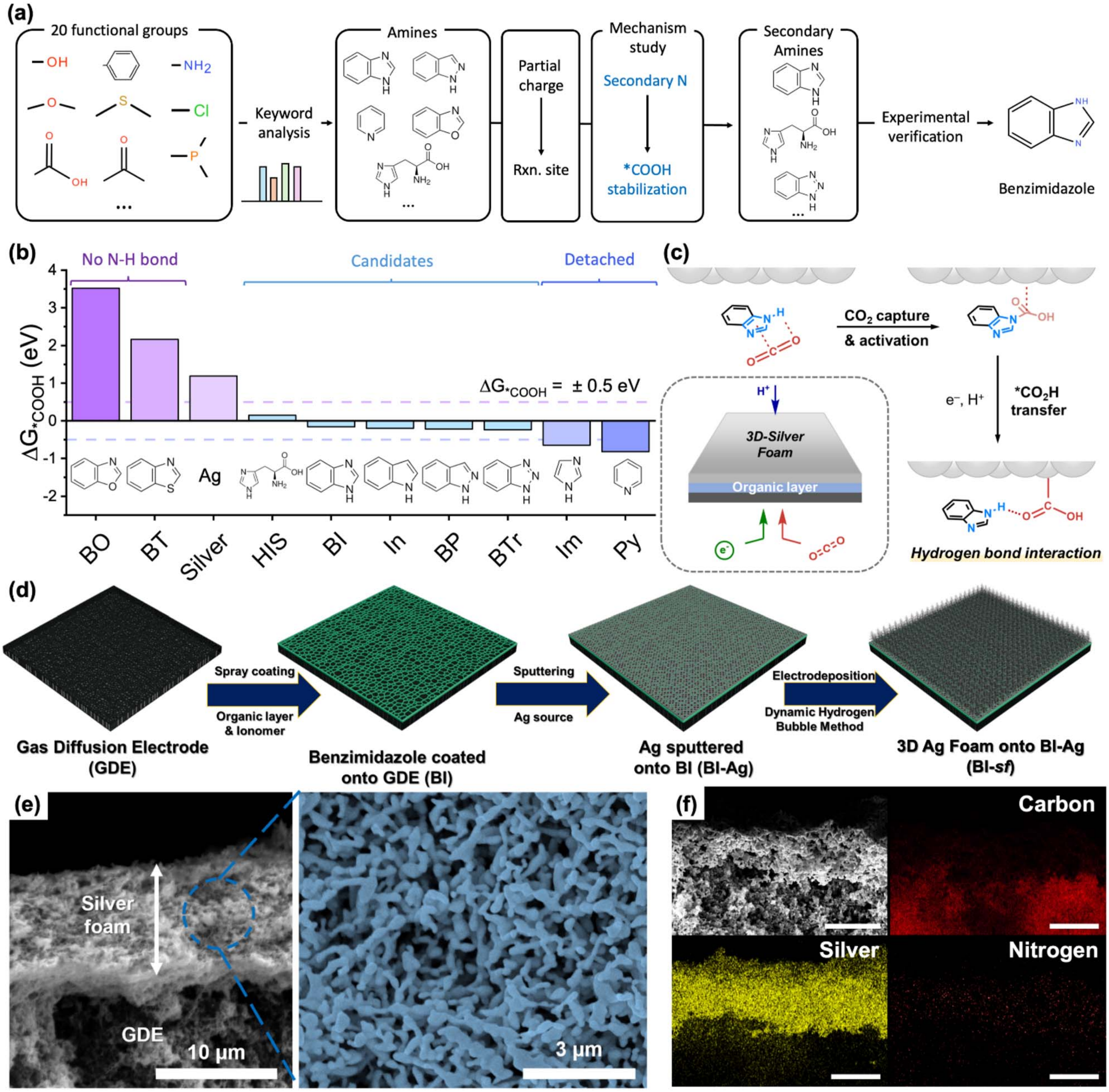

Fig. 1 Structural and interfacial characterization of an organic layer-assisted 3D-Ag foam. Overall screening procedure and mechanism study using DFT. (a) Screening of molecules by keyword analysis, followed by partial charge calculation, mechanism study, and its experimental verification. (b) *COOH adsorption energies of various molecules. Note that OA is discarded in the prior step. (c) Schematic diagram of how the amine functions, including an organic layer that increases local CO_2 availability during electrolysis. (d) Schematic illustration of the fabrication process and working principle of the organic molecule-assisted 3D Ag foam electrode for low-concentration CO_2 electroreduction. (e) Cross-sectional SEM image of the 3D Ag foam electrode onto an organic layer, added GDE (left), and top-viewed SEM image of the electrode (right). (f) EDS mapping of the as-prepared electrode; scale bar: 5 μm.

Ag surfaces. Therefore, we could discard OA as a promising organic candidate. It should be noted that some essential decisions for running DFT calculations (*e.g.*, the relative position and distance between intermediate molecules and amines) were made based on the partial charge analyses of candidate molecules (Fig. S3).

From the consensus that ΔG(*COOH) acts as a major barrier for the CO_2RR to CO on Ag, we set the subsequent descriptor as the adsorption free energy of *COOH, where the amine molecule of interest was also present and placed near *COOH.[42,43] Specifically, molecules having an ΔG(*COOH) >0.5 eV or lower than −0.5 eV were discarded from the candidates. All the relaxed structures are given in Fig. S4. Although the model considered a single molecule on Ag, geometry optimizations from various initial configurations consistently converged to a flat-lying structure due to van der Waals interactions, as shown in Movie S1, thereby supporting the validity of this simplified representation for describing local COOH stabilization. As shown in Fig. 1b, it is notable that secondary amines could stabilize the *COOH intermediate, while the molecules without an N–H bond did not. Moreover, for small molecules such as Im and Py, significant deviations, including molecular detachment, were also observed, which could affect the *COOH adsorption energy and stability in practical organic molecule-assisted CO_2 conversion, as shown in Fig. S4. Given the fact that all the molecules with adequate *COOH binding energy have an N–H bond with *COOH adsorbed near it, we suspect that the stabilization of the *COOH intermediate *via* hydrogen bonding may be an important descriptor for the CO_2RR on metal-adsorbed molecules.

Based on this hypothesis, Fig. 1c schematically illustrates the key chemical steps of this study and our working electrode configuration. First, it is thought that a pre-adsorbed organic molecule can assist in binding CO_2 *via* a chemical step, followed by a proton-coupled electron transfer step resulting in a *COOH intermediate adsorbed on Ag, which is stabilized *via* the hydrogen bond between the O of *COOH and a hydrogen atom of the molecule. Further details on the reaction insights, including DFT calculations, are given in the final section.

Introduction of the organic interlayer plays a decisive part in governing the surface chemistry and reaction microenvironment during CO_2RR. The organic molecules in this work contained polar functional groups, primarily amine (–NH) moieties, that (i) promote selective CO_2 adsorption and (ii) regulate local proton availability. The amine groups form transient carbamate-like intermediates with CO_2, effectively concentrating the gas at the catalyst interface even under low CO_2 partial pressures.

Next, the introduction process for the organic molecule layer on the GDE was designed, as shown in Fig. 1d. The organic molecules were entrapped between the porous GDE and the sputtered Ag thin film layer, where they encountered the supplied CO_2 gas before the Ag catalyst on the cathode. To increase the amount of active Ag electrocatalyst, three-dimensional silver foam (3D-Ag foam) was electrochemically deposited on top of the sputtered Ag thin film.[44] The electrodeposited Ag foam was designed to have a porous morphology, providing diffusion pathways for CO_2 gas, which is essential if mass transfer under diluted conditions limits the partial current density for CO_2RR. The organic molecules were deposited onto the GDE surface by spraying an ink solution containing the molecules and Nafion ionomers. Subsequently, an Ag thin film (5–10 nm) was sputtered onto the organic molecule added to the GDE surface. This process resulted in a uniformly coated electrode, and Fig. S5a shows the case where BI was applied as the organic molecule (BI-Ag). According to our DFT simulation in Fig. 1b, BI was a promising cocatalyst candidate for the CO_2 binding-assisted conversion scenario because its binding affinity is near zero. Ag sputtering also improved the electrical contact of the GDE substrate, facilitating the growth of 3D-Ag foam using the dynamic hydrogen-bubble template (DHBT) method. The 3D porous interconnected Ag foam over the BI-coated GDE (BI-*sf*) is shown in Fig. S5b. The cross-sectional and top-view FESEM images of BI-*sf* showed the porous 3D-Ag morphology over the GDE electrode (Fig. 1e). The EDS spectrum and elemental mapping images of BI-*sf* confirmed that Ag was uniformly distributed throughout Ag foam regions, while carbon was primarily present in the GDE region of the carbon paper. Additionally, a trim level of nitrogen was detectable (Fig. 1f and S6–S8).

Structural characterization of the organic molecule BI on electrodes

The electrode surface was further analyzed to determine whether BI molecules remained on the electrode after Ag loading *via* sputtering or electrodeposition (Fig. 2). FT-IR spectroscopy was performed to identify the characteristic vibrational features of the functional groups in BI (Fig. 2a and b). To prevent IR spectral interference from the carbon paper substrate, BI-Ag was prepared using the same procedure, but with a Ni foil substrate instead. Since the organic layer peaks were obscured by the thick Ag foam deposited on the electrode, the spectra were compared using only the electrode after Ag sputtering. The FT-IR spectra of the BI-Ag were consistent with pure BI molecules, showing strong similarities in features. This finding confirmed that BI molecules were present on the electrode even after Ag sputtering. Notably, blueshifts were observed in the BI-Ag spectrum at 1477 and 1003 cm^{-1}, compared with the reference BI features at 1482 and 1006 cm^{-1}, respectively. These features were assigned to the ring C–C vibration and C–C bending motion, which shift to higher frequencies upon metal coordination. Therefore, the observed blueshifts in BI-Ag suggested that BI interacted with the sputtered Ag film. Furthermore, the BI-Ag prepared on the carbon paper GDE was analyzed by Raman spectroscopy, which allowed the use of the carbon paper substrate. The Raman spectra of the pure-BI gas diffusion electrode (GDE), the sputtered Ag film on the Nafion-coated GDE (GDE-Ag), and BI-Ag on the GDE are shown in Fig. 2c. To confirm that BI was successfully incorporated, GDE and GDE-Ag were used as controls. The Raman spectrum of BI-Ag exhibited clear emergence of two peaks associated with BI (775.9 and 1275.1 cm^{-1}) in addition to the Raman features of D- and G-bands of the carbon substrate. Again, this finding suggested the presence of BI molecules in our BI-Ag electrode after Ag film deposition on the GDE substrate. Additionally, XRD profiles of the Ag foam without BI (denoted as *sf*) and BI-*sf* samples revealed that the diffraction patterns corresponded to Ag (JCPDS no. 03-0921), as marked in Fig. 2d. Four intense peaks appeared at 2θ angles of 37.87°, 44.02°, 64.24°, and 77.24°, corresponding to the *hkl* values of 111, 200, 220, and 311 planes, respectively, indicating an fcc crystal structure. Due to the relatively thick Ag foam compared with the organic BI layer, detectable pattern shifts were not observed; all samples exhibited metallic properties without significant strains in Ag foam.

The XPS analysis of *sf* and BI-*sf* confirmed the presence of the N signal only when BI was introduced. Ag 3d and N 1s spectra provided detailed information on their electronic structure and chemical compositions, as shown in Fig. 2e and f.

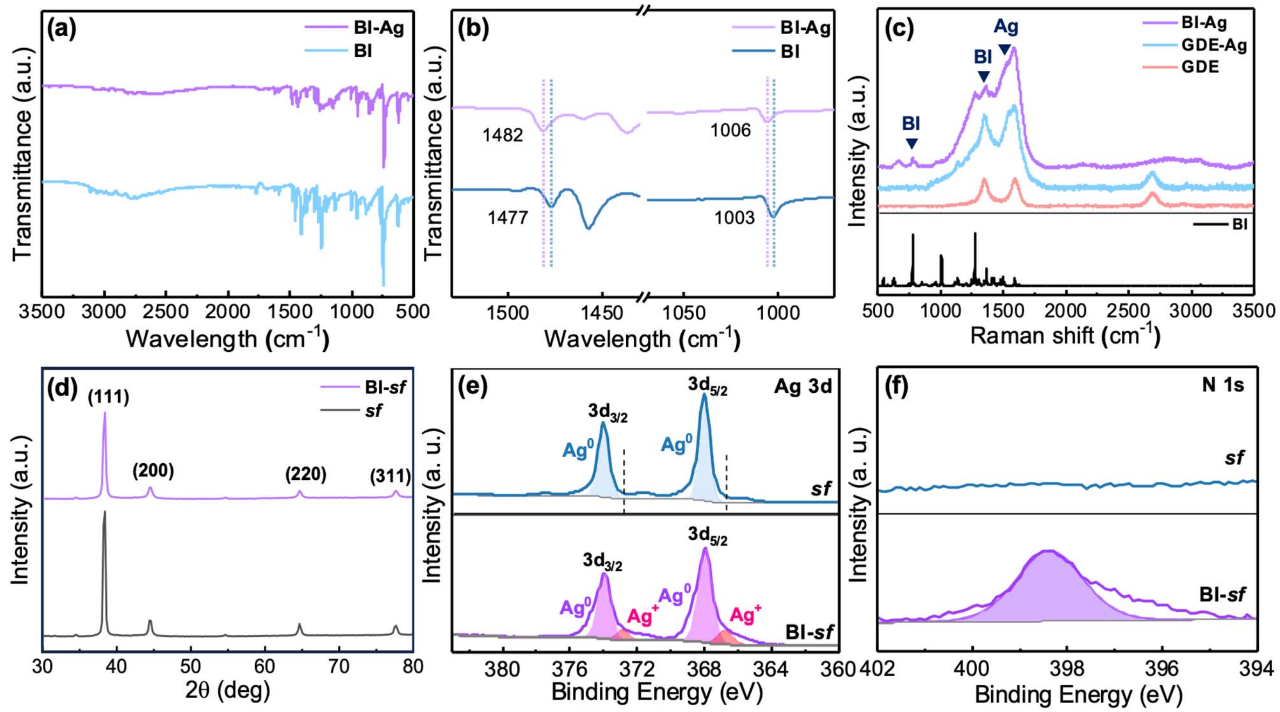

Fig. 2 Structural characterization of the organic molecule BI on electrodes. (a) FT-IR spectrum of the BI molecule and BI-Ag, and (b) its enlarged spectra, and (c) Raman spectrum of GDE, sputtered Ag film onto Nafion-coated GDE (GDE-Ag), and BI-*sf*. (d) X-ray diffraction spectrum and X-ray photoelectron spectrum for (e) Ag 3d, and (f) N 1s of *sf* and BI-*sf*.

Compared with *sf*, BI-*sf* showed broader features with peaks at higher binding energies, implying BI-*sf* had Ag^0 and Ag^+ states. This finding reflected the interaction between Ag and the organic layer, consistent with DFT simulation results in Fig. 1b. In Fig. 2f, the presence or absence of a nitrogen peak further confirmed the incorporation of the organic layer, depending on its addition. Overall, these surface analyses demonstrate that BI was well integrated after fabrication of 3D-silver foam.

Electrochemical CO_2 reduction enabled by a CO_2-affinitive interfacial modifier

Following confirmation of the organic layer, further investigations centred on whether the organic layer could influence CO_2RR performance in the diffusion-controlled region. Initially, linear sweep voltammetry (LSV) curves of the *sf* and BI-*sf* electrodes were acquired with a zero-gap MEA setup under N_2 and CO_2 flow conditions (Fig. 3a). The affinity of the silver active sites for CO_2 could be inferred approximately from comparison of current density profiles under N_2 and CO_2 atmospheres. The *sf* and BI-*sf* electrodes exhibited higher current densities under CO_2RR conditions compared with the HER in an N_2 atmosphere, indicating that the silver foam provided an environment in which CO_2 activation was more feasible than H_2 formation. The BI-*sf* electrode demonstrated a more noticeable increase in current density when switching from N_2 to CO_2 compared with the bare *sf* when BI was absent. This finding indicated that the BI layer contributed to the CO_2 reduction reaction rate (as estimated in Fig. 1) due to its improved CO_2 affinity relative to bare Ag. The improved CO_2RR rate was indicated by the onset potential of the BI-*sf* (−2.2 V), which was nearly 100 mV less negative than that of the *sf* electrode. Additionally, the current density increased more evidently for the BI-*sf* electrode than without BI, based on the differences in the initial slope between N_2 and CO_2 atmospheres. This finding suggested that entrapping organic molecules on the cathode surface supported CO_2RR by increasing its affinity for CO_2, enabling it to supply CO_2 more readily.

The CO_2RR-to-CO conversion activity was more carefully compared with the product analysis under chronopotentiometry (CP) measurements until 800 mA cm^{-2} (Fig. 3b), where the high current density conditions drive the HER instead of CO. BI-*sf* and *sf* electrodes showed high selectivity toward CO in comparison with the HER as the current density was increased up to 300 mA cm^{-2}. However, at high current densities where CO_2 depletion rates may quickly outstrip CO_2 supply rates, CO_2 mass transport limits conversion at Ag active sites even in direct CO_2 gas-fed MEA conditions. This, in turn, allows increases in the competing HER selectivity. The BI-*sf* electrode showed high CO_2RR selectivity (∼95%) up to 500 mA cm^{-2}, while the *sf* electrode exhibited a sharp decline in FE of CO production when the current density increased beyond 400 mA cm^{-2}. These distinctive selectivity differences signified that BI-*sf* could mitigate the mass transfer limit. This effect was again attributed to increased CO_2 accessibility due to the BI interlayer. To elucidate the effect of benzimidazole (BI) on the reaction interface, we investigated three configurations: (i) BI coated on the surface of the porous Ag foam; (ii) BI inserted

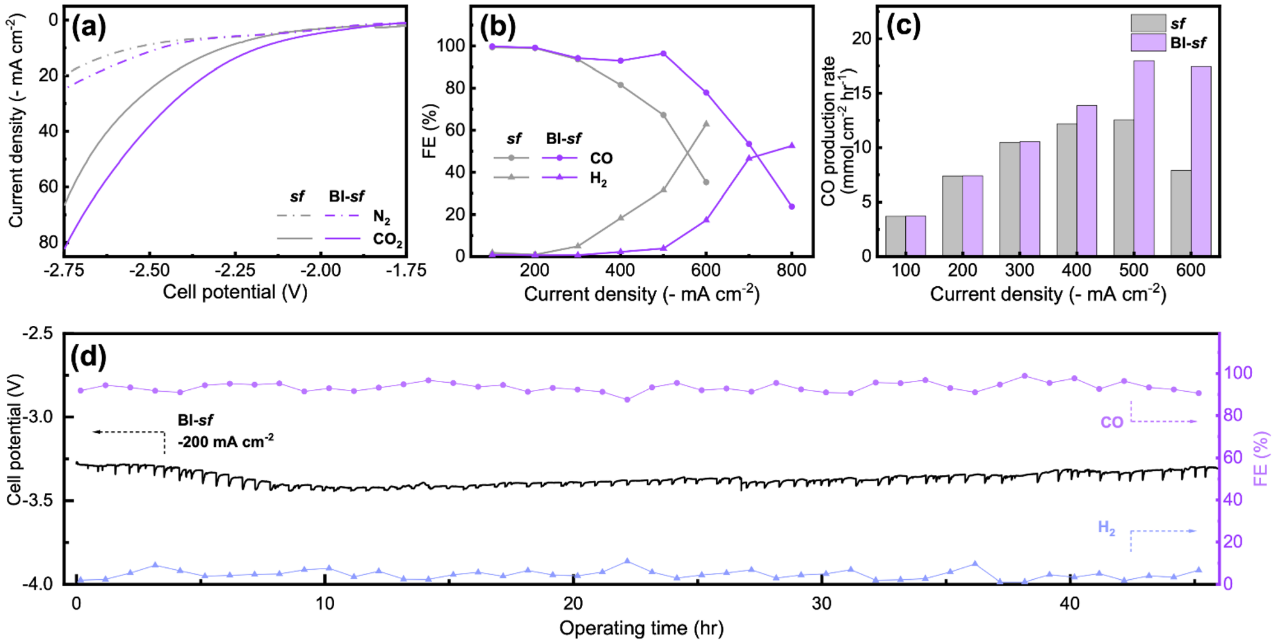

Fig. 3 CO_2-affinitive interfacial modifier-assisted electrochemical performances. (a) LSV for Bi-*sf* (purple lines) and *sf* (gray lines) under CO_2 (solid lines) and an N_2 (dashed lines) atmosphere. (b) FE for CO (round scatter) and H_2 (triangle scatter) production by Bi-*sf* (purple scatter) and *sf* (gray scatter) as a function of controlled current densities. (c) CO production rate for Bi-*sf* (pink column) and *sf* (gray column) as a function of controlled current densities. (d) Long-term continuous CO_2RR with the Bi-*sf* electrode at -200 mA cm^{-2}. Black line: cell potential as a function of reaction time; pink and purple scatters: FE for CO (round scatter) and H_2 (triangle scatter) production.

between the gas diffusion substrate and the Ag layer; (iii) BI applied to both locations (as shown in Fig. S9). Direct coating of BI onto the porous Ag structure led to inferior performance, which we attributed to inhibited interfacial proton transfer due to the hydrophobic nature of BI. In contrast, positioning the BI layer at the substrate–Ag interface effectively increased the local CO_2 environment from the gas flow while preserving accessible Ag active sites for subsequent electrochemical conversion. This configuration also maintained favourable gas transport while minimizing the kinetic penalties associated with excessive surface coverage. Therefore, the interfacial placement of BI was chosen as the optimal strategy rather than a limitation of the fabrication process.

In Fig. 3c, this contrast is even more prominent in the comparison of the CO production rate. It is notable that BI-*sf* and *sf* electrodes produced similar amounts of CO in the lower current-density regions, up to 300 mA cm^{-2}, indicating that the BI layer did not make a significant difference to CO_2RR activity if the amount of CO_2 conversion was low. As the current density increased, the *sf* electrode suffered from increasing HER competition. However, when the BI layer was present, its attraction for CO_2 enhanced CO_2 accessibility to Ag active sites, effectively delaying the mass-transfer limit and achieving a current density (j_{CO}) of 482 mA cm^{-2} with 96% selectivity. Such a trait makes the BI interlayer configuration a novel strategy for CO_2RR electrocatalysts operating under industry-relevant, high-current-density conditions. According to the LSV measurement, the catalytic current density generated by BI-*sf* at a wide CO_2 concentration range is shown in Fig. S10. Even at a low CO_2 concentration of 10%, the current density of BI-*sf* retained over 45% compared with 100% at 3.25 V. Long-term stability of the BI-*sf* electrode was obtained at -200 mA cm^{-2} during 45 h of MEA operation (Fig. 3d). The resulting FE for CO production was kept at almost 100% during electrolysis, indicating structural stability of the BI-*sf* within the MEA configuration. To verify that the sustained performance arose from structural retention rather than electrode restructuring, post-electrolysis characterizations were conducted after the long-term stability test. SEM (Fig. S11) confirmed that the porous morphology of the BI-*sf* electrode remained intact after electrolysis. XRD patterns before and after operation (Fig. S12) did not show detectable phase changes, indicating preservation of the Ag crystalline structure. These results indicated that the long-term stability observed in Fig. 3d originated from minimal structural and interfacial changes during high-current-density MEA operation. Electrochemical impedance spectroscopy (EIS) was performed to compare the interfacial charge-transfer properties of the AgNP-coated electrode, *sf*, and BI-*sf*. As shown in Fig. S13, Nyquist plots revealed pronounced differences in charge-transfer resistance (R_{ct}). The AgNP-coated electrode exhibited a relatively large R_{ct} (0.93 Ω), indicating sluggish charge transfer. In contrast, *sf* showed a markedly lower R_{ct} (0.034 Ω), highlighting the advantage of the three-dimensional porous Ag structure over a simple AgNP coating. BI-*sf* displayed an intermediate R_{ct} (0.065 Ω), remaining substantially lower than that of the AgNP-coated electrode, which indicated that the benzimidazole interlayer did not significantly hinder interfacial charge transfer. The comparable surface resistance (R_s ≈ 0.2–0.28 Ω) confirmed that these differences arose primarily from interfacial effects rather than ohmic losses.

CO_2RR performance comparison under various concentrations of CO_2

The increased CO_2 accessibility effect of the organic molecule interlayer was further investigated to determine whether its promoting effect on CO_2RR was valid under diluted CO_2 conditions and with other organic molecules. The schematic diagram of Fig. 4a illustrated the increased CO_2 transfer mediated by the BI organic molecule layer, which pre-emptively interacted with CO_2 molecules. Before we screened the effect of organic molecules, we first compared the catalytic current density and FE depending on the Ag structure and deposition method on the GDE to select the Ag deposition conditions under diluted CO_2 conditions (Fig. 4b–d). j_{CO} and FE were investigated to determine whether the Ag structure affected the product selectivity between CO and H_2 under diluted CO_2 conditions. Electrodes coated with Ag nanoparticles, sputtered Ag thin film, and Ag foam, referred to as *sf*, were all prepared on the GDE carbon paper. j_{CO} and FE were measured at three cell

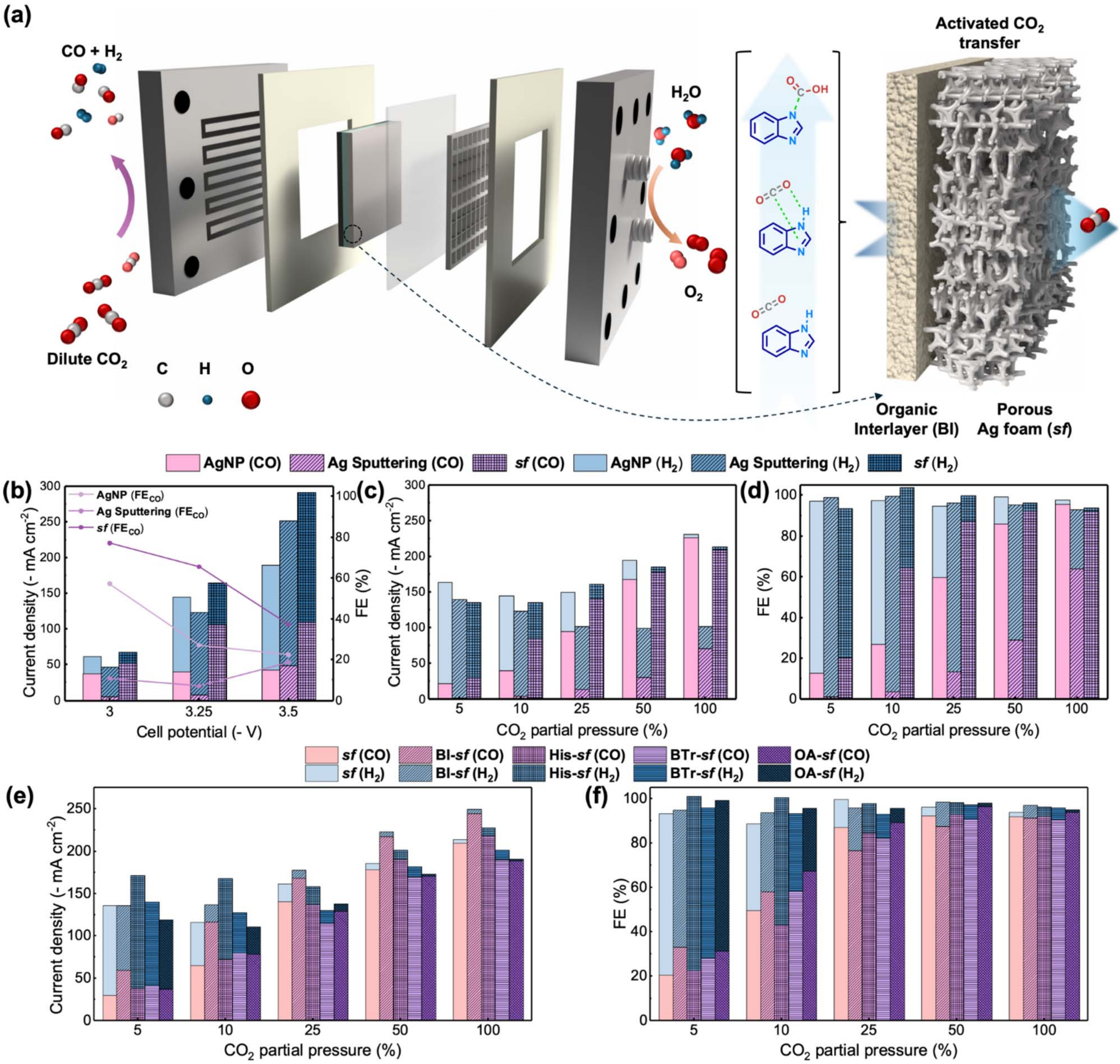

Fig. 4 Comparison of CO_2RR performance under various concentrations of CO_2 conditions. (a) Schematic illustration for CO_2RR electrolysis with Bi-*sf* in a MEA electrolyzer. (b) Current densities and faradaic efficiencies (FE) of AgNP, sputtered Ag, and Ag foam electrodes on GDE carbon paper as a function of the controlled cell potential. (c) Current densities and (d) FE of Ag NP, sputtered Ag, and Ag foam measured at −3.25 V cell potential as a function of the CO_2 concentration. (e) Current densities and (f) FE of Ag foam electrodes depending on the addition of an organic molecular layer (BI, HIS, BTr, and OA) measured at −3.25 V cell potential as a function of CO_2 concentration.

potentials (*i.e.*, 3, 3.25, and 3.5 V) under 10% and 100% CO_2 concentrations, respectively, as shown in Fig. 4b and S14. At 10% CO_2 concentration, the Ag foam (*sf*) exhibited the highest current density and CO selectivity, probably owing to its highly porous structure with thick 3D morphology. In contrast, the thin sputtered Ag layer was not sufficient to convert CO_2 effectively, resulting in the lowest CO selectivity. The AgNP electrode, in which a commercial AgNP ink was sprayed onto the GDE, showed moderate decreases in current density and CO selectivity. Among the three types of Ag electrodes, Ag foam was the optimized structure for achieving the highest j_{CO} and FE(CO), especially under diluted CO_2 conditions. Additionally, at three potentials, −3.25 V showed a notable increase in CO current density compared with that at −3.0 V, but a more negative voltage of −3.5 V increased the HER more than CO_2RR.

After determining the optimal cell potential, the three Ag catalysts were tested under variously diluted CO_2 concentrations (Fig. 4c and d). Notably, FE values remained unchanged at high CO_2 concentrations of 50% and 100%, but declined rapidly as CO_2 level decreased. Among the three catalyst structures, the Ag foam structure best maintained CO selectivity, with only a 1.4-fold decrease (FE(CO) 91.9% → 64.6%) compared with a 3.5-fold decrease (95.7% → 26.9%) for the AgNP-coated electrode and an 18-fold decrease (64.1% → 3.6%) for the sputtered Ag electrode. Regarding individual CO current densities, the Ag foam structure showed the highest CO current ratios between 10% and 100% CO_2 conditions. Specifically, the AgNP-coated and sputtered Ag electrodes retained only 18% ($226.4\ \mathrm{mA\ cm^{-2}} \rightarrow 40.1\ \mathrm{mA\ cm^{-2}}$) and 6% ($70.6\ \mathrm{mA\ cm^{-2}} \rightarrow 4.5\ \mathrm{mA\ cm^{-2}}$) of j_{CO}, respectively. In contrast, the Ag foam maintained 40% of j_{CO} ($209.6\ \mathrm{mA\ cm^{-2}} \rightarrow 84.4\ \mathrm{mA\ cm^{-2}}$), which was remarkable considering the partial pressure of CO_2 decreased by 10-fold between 10% and 100% CO_2 conditions. Therefore, the highly porous nature of the Ag foam structure appeared to positively influence CO_2RR selectivity under diluted CO_2 conditions.

To investigate whether other organic molecules can also assist CO_2 accessibility, Ag foam electrodes with different organic interlayers were systematically tested. Based on preliminary calculations and structural analysis, L-histidine (HIS), benzotriazole (BTr), and octylamine (OA) were selected for screening across a range of CO_2 concentrations from high to low. HIS is another imidazole-containing molecule, and BTr is a member of the benzazole family, with an additional nitrogen atom in the azole ring. OA was selected as a substantially different primary amine source due to its linear, saturated aliphatic chain. At high CO_2 concentrations, all organic molecules showed similar CO selectivity, although HIS-*sf* quickly accelerated HER rates as the CO_2 concentration was lowered. Among the organic molecule candidates, BI-*sf* stood out for retaining the highest CO selectivity and current density. This reactivity was attributed to the nature of the imidazole ring because the N–C═N bond can form carbamates *via* weak N–C bonds. In light of the Sabatier principle, the relatively unstable carbamic acid can easily dissociate back to CO_2, which signifies that partially activated CO_2 can be supplied to the active Ag catalyst.

The CO_2RR performances at high and low CO_2 concentrations of the aforementioned electrodes are summarized in Fig. S15. BI-*sf* showed the highest partial current density at high and low CO_2 conditions. Specifically, the BI interlayer enhanced CO selectivity under diluted CO_2 conditions by improving CO_2 accessibility, showing 58% FE compared with 27% for AgNP. BTr and OA showed selectivity profiles similar to BI, but exhibited lower current density. HIS-*sf* showed high CO selectivity and partial current densities at high CO_2 partial pressures. Although HIS also contains an imidazole ring, the $H_2N–CH(R)–CO_2–$ motif may exist in the zwitterionic form, rendering HIS inherently hydrophilic. Therefore, HER activity becomes more dominant under lower CO_2 conditions. As summarized in Table S2, the BI-*sf* electrode demonstrated competitive CO faradaic efficiency and stable performance compared with those reported for Ag-based MEA systems operating under diluted CO_2 conditions. This comparison indicates that introducing an organic interfacial layer between the substrate and Ag catalyst can help mitigate CO_2 depletion effects and improve operational robustness during long-term testing. To probe the practical lower limit of gas-fed CO_2 electroreduction beyond flue-gas conditions, additional experiments were performed under highly diluted CO_2 conditions (650–5000 ppm) (Table S3).

To better understand the promoting effect of each organic molecule on CO_2RR-to-CO performance, the interaction between molecules and CO_2 was further investigated. First, the charge delocalization throughout an aromatic molecule attached to the Ag surface was visualized (Fig. S16), demonstrating its high CO_2 affinity. For the optimized geometries of candidate molecules adsorbed with *COOH used in screening (Fig. 1b and S4), a simple unit cell composed of 25 silver atoms, the molecules of interest, and the *COOH adsorbate with a Γ-centered Brillouin zone sampling was selected for facile screening. As one can see in the relaxed geometries (Fig. S4), molecules with secondary amines were capable of stable attachment on the Ag surface, while primary and saturated amines were relatively unstable. Moreover, in some cases, such as when pyridine was placed near *COOH, molecular detachment was observed and has had a significant role in lowering the adsorption free energy to an undesired level. For molecules with higher *COOH binding energy than Ag (*e.g.*, benzoxazole), analysis of charge density difference revealed that the repulsion between two electronegative atoms was the driving force for the detachment of molecules from the Ag surface and a significant increase in adsorption energy (Fig. S17). On the contrary, all *COOH adsorption energies for secondary amines decreased compared with that of bare Ag (1.05 eV). Therefore, we focused on the ability of secondary amines for further discussion.

Three secondary amines (BI, BTr, and HIS) that showed satisfactory CO_2RR performances were chosen for further mechanistic study. A bilayer Ag substrate with a fixed bottom layer was introduced, and sampling was increased from a single.

Γ-Point to a Γ-centered 2 × 2 × 1 Brillouin zone. Full reaction pathways from *CO_2 to CO(g) desorption were simulated for three molecules, and the results are shown in Fig. 5a and b. Using BI as a representative molecule, the reaction mechanism

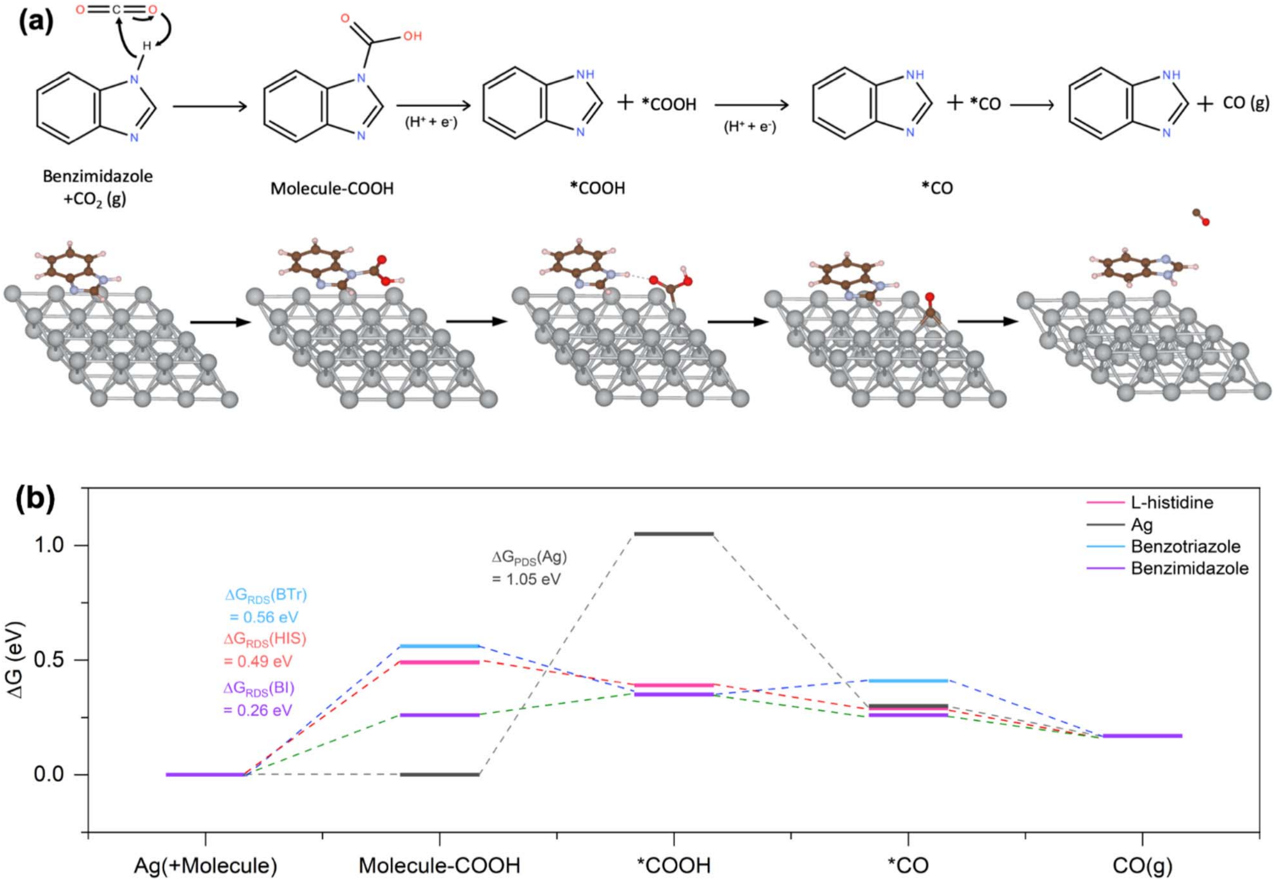

Fig. 5 (a) Mechanism of CO_2RR on the benzimidazole-adsorbed Ag surface and the corresponding geometry-optimized structure. Atoms in the structural scheme are represented in different colors (brown: C; white: H; sky-blue: N; red: O; gray: Ag). (b) A free energy diagram showing the electrocatalytic reaction pathways on three types of organic molecules (BI, BTr, HIS) and bare silver.

is presented in Fig. 5a. First, the CO_2 molecule is thought to be polarized and forms carbamic acid because the secondary N in BI has the most negative partial charge according to the simulation (Fig. S3). Afterwards, *via* a proton-coupled electron transfer (PCET) step, the *COOH is adsorbed directly next to the recovered molecule, benzimidazole. In this step, it is thought that an H-bond between hydrogen from benzimidazole and O from *COOH could be formed, which contributes to lowering the adsorption free energy of *COOH. In a subsequent PCET step, the *COOH becomes *CO and is finally released in the gaseous form.

Fig. 5b shows the reaction pathway for three molecules. Compared with the reaction pathways of Ag, these molecules significantly lowered the Δ*G*_(*COOH), shifting the rate-determining step from *COOH adsorption to carbamic acid formation, which was significantly lower than Δ*G*_(*COOH) of Ag. From the optimized structure of the *COOH-adsorbed Ag surface with BI (Fig. 5a and S4), it was again notable that the distance between H from the secondary amine of benzimidazole and O from the *COOH intermediate was 1.84 Å, which falls in a range of typical hydrogen bond length.[45] A charge density difference plot of the structure (Fig. S18) also ensured the interaction between hydrogen and oxygen, where the electron-rich region is depicted in yellow, and the electron-deficient region is depicted in blue.

For the quantitative examination of *COOH intermediate stabilization behavior with H-bonding, crystal orbital Hamiltonian population (COHP) calculations were conducted (Fig. S19).[40] In detail, the negative-signed integration of COHP from negative infinity to Fermi energy, known as –ICOHP, was used as a quantitative measure of bond strength. As a result, the –ICOHP of −0.65 eV indicates a hydrogen bond, but also corresponds well with the reported hydrogen bond strength of N–H⋯O.[45] Thus, we concluded that the formation of a hydrogen bond between the *COOH intermediate and benzimidazole was feasible but also could contribute to stabilization of the *COOH intermediate on the Ag surface.

We propose that the hybrid molecular-inorganic catalyst design demonstrated a unique ability to preserve high CO selectivity and activity even under dilute CO_2 concentrations, where traditional Ag-based electrocatalysts typically experience a dominant increase in HER activity due to the limited mass transport of CO_2. The 3D Ag foam structure provides highly efficient gas electron transport and increases the electrochemically accessible surface area, resulting in improved reaction kinetics compared with conventional planar Ag catalysts.

Integrating a 3D Ag foam structure with an interfacial organic benzimidazole layer enhances CO_2 affinity through reversible chemisorption and hydrogen-bonding interactions, mitigating the diffusion-controlled conversion rate. Additionally, the integration process is simple and solution-processable, compatible with MEA systems, and offers insights into practical catalyst design for the industrial CO_2-to-CO conversion under diluted CO_2 conditions.

Conclusions

We demonstrated that embedding a CO_2-affinitive benzimidazole interlayer beneath a 3D-Ag foam catalyst enabled highly efficient CO_2 electroreduction even under industrially relevant, low-concentration CO_2 conditions. The organic layer enhanced local CO_2 availability through reversible CO_2-affinitive interactions while stabilizing the *COOH intermediate with hydrogen bonding, thereby shifting the rate-determining step and reducing competing HER. Coupled with the high surface area and fast gas-electron transport pathways of the 3D Ag foam, the BI-*sf* electrode achieved high maximum CO partial current densities and faradaic efficiencies across a wide range of CO_2 concentrations, maintaining selectivity. Inclusion of the BI layer promoted CO_2RR activity, particularly under mass transport control conditions, while CO production activity remained similar at low current densities, because BI acted as a cocatalyst to improve CO_2 accessibility near the Ag surface. Compared with commercial AgNP, the BI-*sf* electrode exhibited a 2.5-fold and 4-fold partial current density in 100% and 10% CO_2 conditions, respectively. Furthermore, BI-*sf* showed the highest j_{CO} and FE for CO production at CO_2 concentrations diluted within the 50–5% range, demonstrating a particular promoting effect under mass transport control conditions. This molecular-interfacial design strategy employs a rational organic–inorganic combination and is fully compatible with scalable MEA electrolyzer architectures, providing a practical pathway for direct CO production from diluted CO_2 streams and significantly advancing the feasibility of carbon capture-integrated electrochemical utilization.

Author contributions

Kyeong-Nam Kang: writing-original draft, validation, methodology, investigation, data curation, formal analysis. Dongyoon Shin: investigation, data curation, formal analysis, writing: original draft. Jihoon Kim: investigation, calculation, writing: original draft. Sang Heon Han: investigation, formal analysis. Jiseon Kim: data acquisition, investigation. Kyung Taek Woo: investigation, funding acquisition. Seoungsoo Park: investigation funding acquisition. YunJeong Hwang: writing: review & editing, supervision, project administration, funding acquisition, conceptualization, investigation.

Conflicts of interest

There are no conflicts to declare.

Data availability

Additional data are available from the corresponding author upon reasonable request.

The data supporting the findings of this study are available within the article and its supplementary information (SI) files. Supplementary information is available. See DOI: https://doi.org/10.1039/d5ta08633g.

Acknowledgements

The authors acknowledge the financial support of the KOGAS R&D Institute, Korea Gas Corporation (RD2023-0281).

Notes and references

1 J. Resasco and A. T. Bell, *Trends Chem.*, 2020, **2**, 825–836.
2 Y. Y. Birdja, E. Pérez-Gallent, M. C. Figueiredo, A. J. Göttle, F. Calle-Vallejo and M. T. M. Koper, *Nat. Energy*, 2019, **4**, 732–745.
3 Y. J. Sa, C. W. Lee, S. Y. Lee, J. Na, U. Lee and Y. J. Hwang, *Chem. Soc. Rev.*, 2020, **49**, 6632–6665.
4 S. Nitopi, E. Bertheussen, S. B. Scott, X. Liu, A. K. Engstfeld, S. Horch, B. Seger, I. E. L. Stephens, K. Chan, C. Hahn, J. K. Nørskov, T. F. Jaramillo and I. Chorkendorff, *Chem. Rev.*, 2019, **119**, 7610–7672.
5 A. Goyal, G. Marcandalli, V. A. Mints and M. T. M. Koper, *J. Am. Chem. Soc.*, 2020, **142**, 4154–4161.
6 F. Yu, K. Deng, M. Du, W. Wang, F. Liu and D. Liang, *Carbon Capture Sci. Technol.*, 2023, **6**, 100081.
7 R. Sun, J. Zhao and X. Lu, *J. Mater. Chem. A*, 2024, **12**, 8429–8437.
8 M. Li, E. Irtem, H.-P. Iglesias van Montfort, M. Abdinejad and T. Burdyny, *Nat. Commun.*, 2022, **13**, 5398.
9 D. A. Henckel, P. Saha, S. Rajana, C. Baez-Cotto, A. K. Taylor, Z. Liu, M. G. Resch, R. I. Masel and K. C. Neyerlin, *ACS Energy Lett.*, 2024, **9**, 3433–3439.
10 J. Osiewacz, M. Löffelholz, B. Ellendorff and T. Turek, *J. Power Sources*, 2024, **603**, 234430.
11 S. Zhao, R. Jin and R. Jin, *ACS Energy Lett.*, 2018, **3**, 452–462.
12 X. Zhang, S.-X. Guo, K. A. Gandionco, A. M. Bond and J. Zhang, *Mater. Today Adv.*, 2020, **7**, 100074.
13 X. Li, X. Wu, X. Lv, J. Wang and H. B. Wu, *Chem Catal.*, 2022, **2**, 262–291.
14 H. Wu, A. Singh-Morgan, K. Qi, Z. Zeng, V. Mougel and D. Voiry, *ACS Catal.*, 2023, **13**, 5375–5396.
15 X. Zhu, J. Huang and M. Eikerling, *ACS Catal.*, 2021, **11**, 14521–14532.
16 B. Kim, S. Ma, H.-R. Molly Jhong and P. J. A. Kenis, *Electrochim. Acta*, 2015, **166**, 271–276.
17 M. Khalil, G. T. M. Kadja, F. A. A. Nugroho, L. G. Sutanto, P. K. Jiwanti, F. F. Abdi, F. Hussin and M. K. Aroua, *Renewable Sustainable Energy Rev.*, 2024, **206**, 114869.
18 S. Yoo, D. Kim, G. Deng, Y. Chen, K. Lee, S. Yoo, X. Liu, Q. Tang, Y. J. Hwang, T. Hyeon and M. S. Bootharaju, *J. Am. Chem. Soc.*, 2025, **147**, 12546–12554.

19 S. Yoo, S. Park, J. Son, J. Kim, H. Shin and Y. J. Hwang, *J. Am. Chem. Soc.*, 2025, **147**, 12996–13007.

20 Z. Xing, L. Hu, D. S. Ripatti, X. Hu and X. Feng, *Nat. Commun.*, 2021, **12**, 136.

21 K. A. Adegoke and P. F. Tseki, *J. CO2 Util.*, 2025, **101**, 103201.

22 G. Li, Y. Liu, T. Feng and R. Ye, *ChemElectroChem*, 2024, **11**, e202400475.

23 L. Xie, Y. Cai, Y. Jiang, M. Shen, J. C.-H. Lam, J.-j. Zhu and W. Zhu, *Nat. Commun.*, 2024, **15**, 10386.

24 R. V. Mom, L.-E. Sandoval-Diaz, D. Gao, C.-H. Chuang, E. A. Carbonio, T. E. Jones, R. Arrigo, D. Ivanov, M. Hävecker, B. Roldan Cuenya, R. Schlögl, T. Lunkenbein, A. Knop-Gericke and J.-J. Velasco-Vélez, *ACS Appl. Mater. Interfaces*, 2023, **15**, 30052–30059.

25 D. Song, Y. Lian, M. Wang, Y. Su, F. Lyu, Z. Deng and Y. Peng, *eScience*, 2023, **3**, 100097.

26 D. V. Vasilyev and P. J. Dyson, *ACS Catal.*, 2021, **11**, 1392–1405.

27 A. Thevenon, A. Rosas-Hernández, A. M. Fontani Herreros, T. Agapie and J. C. Peters, *ACS Catal.*, 2021, **11**, 4530–4537.

28 M. Melchionna, P. Fornasiero, M. Prato and M. Bonchio, *Energy Environ. Sci.*, 2021, **14**, 5816–5833.

29 L. Xue, Z. Gao, T. Ning, W. Li, J. Li, J. Yin, L. Xiao, G. Wang and L. Zhuang, *Angew. Chem., Int. Ed.*, 2023, **62**, e202309519.

30 W. Jung, S.-H. Shin, S. Park, Y. Chae, U. Lee, H. J. Cho, S. Kim, Y. J. Hwang, J. Y. Lee and D. H. Won, *ACS Energy Lett.*, 2025, **10**, 620–628.

31 M. Fan, J. E. Huang, R. K. Miao, Y. Mao, P. Ou, F. Li, X.-Y. Li, Y. Cao, Z. Zhang, J. Zhang, Y. Yan, A. Ozden, W. Ni, Y. Wang, Y. Zhao, Z. Chen, B. Khatir, C. P. O'Brien, Y. Xu, Y. C. Xiao, G. I. N. Waterhouse, K. Golovin, Z. Wang, E. H. Sargent and D. Sinton, *Nat. Catal.*, 2023, **6**, 763–772.

32 L. Hu, J. A. Wrubel, C. M. Baez-Cotto, F. Intia, J. H. Park, A. J. Kropf, N. Kariuki, Z. Huang, A. Farghaly, L. Amichi, P. Saha, L. Tao, D. A. Cullen, D. J. Myers, M. S. Ferrandon and K. C. Neyerlin, *Nat. Commun.*, 2023, **14**, 7605.

33 L. Ge, H. Rabiee, M. Li, S. Subramanian, Y. Zheng, J. H. Lee, T. Burdyny and H. Wang, *Chem*, 2022, **8**, 663–692.

34 J. Gasteiger and M. Marsili, *Tetrahedron*, 1980, **36**, 3219–3228.

35 P. Giannozzi, S. Baroni, N. Bonini, M. Calandra, R. Car, C. Cavazzoni, D. Ceresoli, G. L. Chiarotti, M. Cococcioni, I. Dabo, A. Dal Corso, S. de Gironcoli, S. Fabris, G. Fratesi, R. Gebauer, U. Gerstmann, C. Gougoussis, A. Kokalj, M. Lazzeri, L. Martin-Samos, N. Marzari, F. Mauri, R. Mazzarello, S. Paolini, A. Pasquarello, L. Paulatto, C. Sbraccia, S. Scandolo, G. Sclauzero, A. P. Seitsonen, A. Smogunov, P. Umari and R. M. Wentzcovitch, *J. Phys.: Condens. Matter*, 2009, **21**, 395502.

36 J. P. Perdew, K. Burke and M. Ernzerhof, *Phys. Rev. Lett.*, 1996, **77**, 3865–3868.

37 S. Grimme, J. Antony, S. Ehrlich and H. Krieg, *J. Chem. Phys.*, 2010, **132**, 154104.

38 P. E. Blöchl, *Phys. Rev. B*, 1994, **50**, 17953–17979.

39 V. L. Deringer, A. L. Tchougréeff and R. Dronskowski, *J. Phys. Chem. A*, 2011, **115**, 5461–5466.

40 J. F. Burnham, *Biomed. Digit. Libr.*, 2006, **3**, 1.

41 E. Prosen and R. Sachs, *Phys. Rev.*, 1942, **61**, 65.

42 Y. Hori, H. Wakebe, T. Tsukamoto and O. Koga, *Electrochim. Acta*, 1994, **39**, 1833–1839.

43 S. Back, M. S. Yeom and Y. Jung, *ACS Catal.*, 2015, **5**, 5089–5096.

44 K.-N. Kang, A. Ramadoss, J.-W. Min, J.-C. Yoon, D. Lee, S. J. Kang and J.-H. Jang, *Nano-Micro Lett.*, 2020, **12**, 28.

45 V. L. Deringer, U. Englert and R. Dronskowski, *Chem. Commun.*, 2014, **50**, 11547–11549.